Runup of solitary waves on a circular island

By PHILIP L.-F. LIU[1], YONG-SIK CHO[1],
MICHAEL J. BRIGGS[2], UTKU KANOGLU[3],
AND COSTAS EMMANUEL SYNOLAKIS[3]

[1]School of Civil and Environmental Engineering, Cornell University, Ithaca, NY 14853, USA

[2]Coastal Engineering Research Center, USAE Waterways Experiment Station,
Vicksburg, MS 39180, USA

[3]Department of Civil Engineering, University of Southern California, Los Angeles,
CA 90089-2531, USA

This is a study of the interactions of solitary waves climbing up a circular island. A series of large-scale laboratory experiments with waves of different incident height-to-depth ratios and different crest lengths is described. Detailed two-dimensional run-up height measurements and time histories of surface elevations around the island are presented. A numerical model based on the two-dimensional shallow-water wave equations including runup calculations was developed. Numerical model predictions agreed very well with the laboratory data and the model was used to study wave trapping and the effect of slope. Under certain conditions, enhanced runup and wave trapping on the lee side of the island were observed, suggesting a possible explanation for the devastation reported by field surveys in Babi Island off Flores, Indonesia, and in Okushiri Island, Japan.

1. Introduction

From 1992 to 1994, submarine earthquakes around the Pacific basin generated six large tsunamis: the Nicaragua tsunami on September 2, 1992; the Flores Island tsunami on December 12, 1992; the Hokkaido Island tsunami on July 12, 1993; the East Java tsunami of June 2, 1994; the Kuril Islands tsunami of October 4, 1994; and the Mindoro Island tsunami of November 15, 1994. They all caused extensive property damage and deaths of at least 1640 people (Satake *et al.* 1993; Yeh *et al.* 1993; Hokkaido Tsunami Survey Group 1993; Yeh *et al.* 1995; Synolakis *et al.* 1995; Imamura *et al.* 1995). In the Flores Island and Okushiri events, unexpectedly large tsunami runup heights in the lee of small islands were observed. During the Flores event, two villages located on the southern side of the circular Babi Island, whose diameter is approximately 2 km, were washed away by the tsunami, attacking from the north (see figure 1). Similar phenomena occurred on the pear-shaped Okushiri Island, which is approximately 20 km long and 10 km wide (see figure 2). The southern region of the island suffered extensive damage from the tsunami attack, which approached the island from the northwestern direction. Maximum runup height at the marked location in figure 2 was about 20 m. These phenomena are apparently not entirely uncommon and have also been reported by Bascom (1990): "We discovered that, except for headlands pointing into the (tsunami) wave, embayments facing exactly opposite to the wave direction were likely to be most affected."
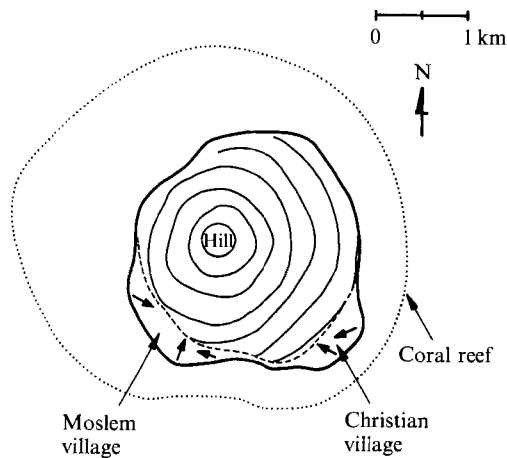
FIGURE 1. A sketch of Babi Island (from Yeh et al. 1994). The 1992 tsunami attacked from the north. Two villages on the lee side of the island were destroyed.
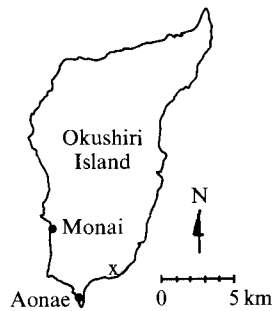

FIGURE 2. A sketch of Okushiri Island of Japan (from Hokkaido Tsunami Survey Group 1993). The 1993 tsunami attacked from the northwestern direction. Maximum runup height reached 30.5 m at Monai which faces the tsunami directly. However, the second largest runup height ($\sim$ 20 m) was observed northeast of Aonae in the lee side of the island indicated by x.

Determination of the runup height distribution along a coastline or around an island is not a trivial problem. It involves not only the three-dimensional motion of a free boundary, but is also highly dependent on the accuracy of bathymetric and topographic data, and on the initial tsunami-profile data which, in turn, depend on the fault solution for the earthquake. Yet accurate predictive capability is necessary to model the inundation from past and future hypothetical events. To this end, several numerical models have recently been developed to simulate historical tsunami events (e.g. Liu et al. 1993; Titov & Synolakis 1993; Mader & Bernard 1993; Takahashi, Imamura & Shuto 1993). Computational details of different models will not be discussed in this paper, and a detailed discussion of the tsunami generation and propagation problem on open coastlines will not be presented. Instead, this paper will concentrate on the problem of solitary wave runup on circular islands whose solution provides insight into counterintuitive mechanisms of tsunami inundation.

The problem of water waves refracting around a circular island was first studied by Arthur (1946) and Pocinki (1950) using ray theory. Jonsson and his associates (e.g. Jonsson, Skovgaard & Brink-Kjaer 1976; Jonsson & Skovgaard 1979) computed wave-ray patterns and their amplitude distribution on a circular island for a wide range of incident wave frequencies. In their studies, the island bathymetry was
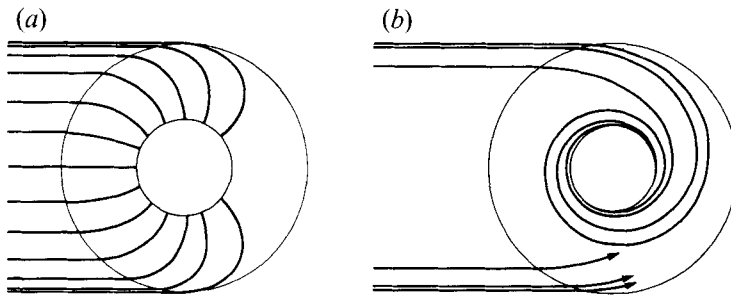
FIGURE 3. (*a*) A sketch of the wave ray patterns for a relatively short wave. A geometric shadow (lee shore) appears in the lee side of the circular island, in which the wave amplitude vanishes. (*b*) Sketch of the wave ray pattern for a relatively long wave. Some rays whirl around the island several times before they reach the shore. Symmetrical rays starting from the lower part are not shown in full.

idealized: it was a cylindrical 'island' situated on a paraboloidal shoal. Along the shoreline $r = r_a$ the water depth h_a is finite. The toe of the island shoal is located at $r = r_b$ where the depth is h_b. Using different incident wave periods, Jonsson and his associates demonstrated different wave ray patterns. For a relative short wave period or when the wavelength is relatively smaller than the island radius, they found that wave rays could not propagate into the geometric shadow or the 'lee shore' named by Arthur (1946) (see figure 3*a*). Wave amplitude was zero in the lee shore. As the wave period increased, the rays from one side of the axis crossed those from the other side in the lee of the island. In some cases, rays whirled around the island several times before they reached the shore (see figure 3*b*). Jonsson and his associates computed the resulting wave amplitude by superposition and proper accounting of the phases. They found that for certain wave periods, the wave amplitude in the lee of the island exceeded that in the front of the island (Jonsson *et al.* 1976).

The ray theory is based on the concept of geometric optics. Therefore, it poses a severe restriction (or idealization) on the bathymetry: the percentage change of the bathymetry within a wavelength has to be very small. As a result, both reflection and diffraction due to bathymetric variations are ignored. To remove some of these limitations, Keller and his associates (e.g. Keller 1958, 1962; Keller & Ahluwalia 1973) developed the geometrical theory of diffraction, which introduced the concept of diffracted rays. Thus, this approach provides an accurate description of wave diffraction in a shadow region behind a structure or in the vicinity of caustics. On the other hand, Lautenbacher (1970), Smith & Sprinks (1975), Jonsson *et al.* (1976), and Jonsson & Skovgaard (1979) have investigated the combined refraction and diffraction of periodic waves by a circular island by using either the linear shallow-water wave theory or the linear mild-slope equation, which is suitable for intermediate water depth. While it is well-justified to assume that modification of tsunamis by bathymetry can be accurately described by linearized equations, tsunami waves are dramatically nonlinear in their final runup phase. Furthermore, all existing linear models stop the calculation at the initial shoreline. Runup invariance for one-dimensional propagation proposed by Carrier (1966) and proved by Synolakis (1987) notwithstanding, there is no evidence to suggest that there is invariance between linear and nonlinear theory for the two-dimensional problem. Moreover, theoretical and numerical solutions are not available for runup heights around a circular island caused by a solitary wave.

The only published experimental data on runup heights of periodic waves on a

circular island are reported by Provis (1975). Provis' experiments were conducted in a small basin (5.55 m wide and 5.80 m long). The base diameter of the island was 3 m and the slope was 1V:10H. The water depth in the constant-depth region in the experiments was 0.15 m. Provis reported large discrepancies between his experimental data and theoretical results predicted by Smith & Sprinks (1975). Sprinks & Smith (1983) pointed out later that because of the relatively small size of the wave basin and the shallow water, viscous damping and standing waves between the wave generator and the island render such comparisons inappropriate.

This paper reports a portion of the results from a combined theoretical and experimental study on the three-dimensional runup of a solitary wave on a circular island. The generation of nearshore tsunamis notwithstanding (Tadepalli & Synolakis 1994), solitary wave profiles are an adequate and useful model for far-field tsunamis. Since they can be described uniquely by a single parameter, they do provide an elegant framework to study complicated multi-parameter phenomena. Experiments were performed in a 30 m wide and 25 m long wave basin, so that boundary effects were minimized, in the sense that the important runup observations took place before waves were reflected from the basin walls. A numerical model developed based on the nonlinear shallow-water equations, and a moving boundary scheme to track shoreline motions are also presented. Bottom friction was also included in the numerical model, although it was not very important for the experiments presented here. Experimental data, including the time histories of free-surface displacements at different locations and maximum runup heights around the island, were used to verify the numerical model. Very good agreement was found and the model was then used to explore in detail other physical phenomena, such as wave trapping around the island, the velocity field, and enhanced runup heights in the lee side of the island.

Section 2 discusses the experimental setup and describes the wave parameters used in the experiments. A brief discussion of the numerical model is given in §3. Detailed information on the numerical scheme and boundary conditions is given in Appendices A and B. Comparisons between numerical solutions and experimental data are presented in §4. Finally, results are discussed and findings are summarized in §5.

2. Laboratory experiments

Experiments were performed in a wave basin at the US Army Engineer Waterways Experiment Station, Coastal Engineering Research Center. The basin is 30 m wide and 25 m long. The centre of the circular island was located at ($x = 15$ m, $y = 13$ m). The slope of the circular island was $14.04°$ (1V:4H slope) and the diameter at the base was 7.2 m. The surface of the island and the floor of the basin were smooth concrete. A directional spectral wave generator (DSWG) was installed along the x-axis (see figure 4) and was used to generate solitary waves. The total length of the wave maker is 27.432 m and it consists of 60 individual paddles moving parallel to the water surface; each of them is independently and electronically driven. A sketch of the island geometry is shown in figure 4. Twenty-seven capacitance wave gauges were used to measure surface-wave elevations; their locations are shown in figure 5, while table 1 lists the coordinates of the first 18 gauges; the other nine can be inferred from symmetry by reference to figure 5.

Two water depths were used in the experiments: 0.32 m and 0.42 m. To investigate the effects of source length of incoming solitary waves on runup heights, different wave maker lengths L were used. As shown in table 2, the ratio of the source length L to the base-diameter of the island D ranged from 0.889 to 3.810. When the ratio is
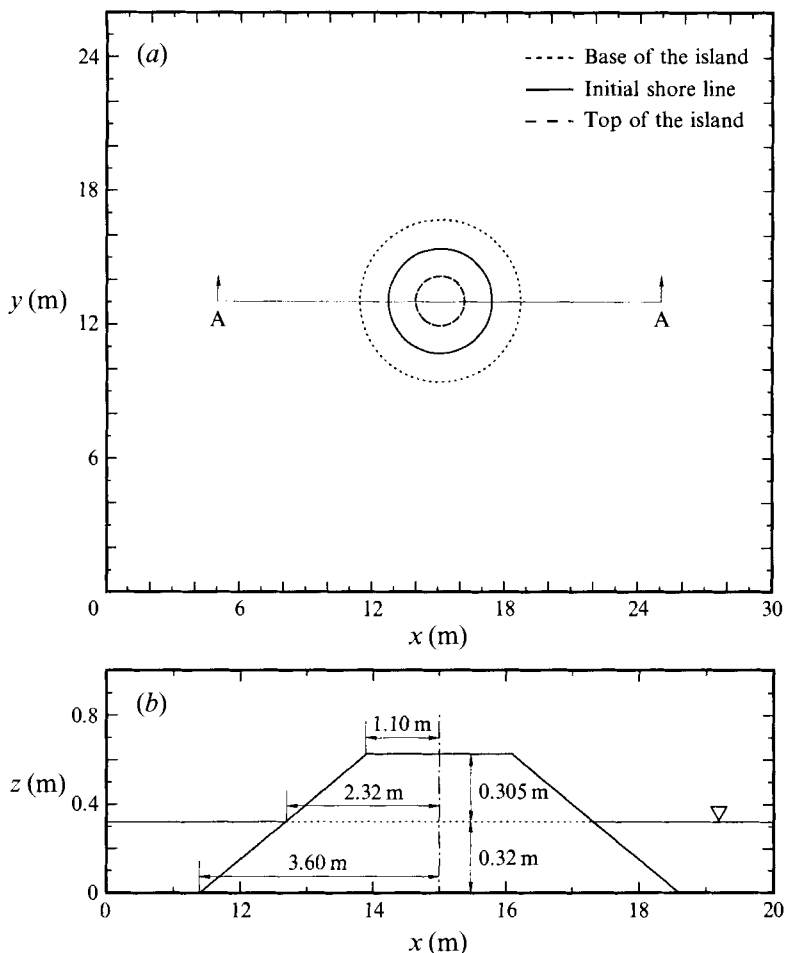
FIGURE 4. (*a*) Top view of the wave basin and the island. (*b*) Vertical view of the circular island on the cross-section A–A.

less than 1, the length of the incident solitary wave (in the transverse direction) is less than the shelf width. The incident wave radiated in the horizontal direction before it reached the island and formed a non-uniform crest line. When the entire length of the wave maker was used (module 4 in table 2), the incident wave form was uniform in the transverse direction.

A measure of the nonlinearity of the incident wave is the height-to-depth ratio of the incident solitary wave, defined as $\epsilon = A/h$ where h is the still-water depth in the constant-depth region of the tank. In these experiments, $h = 0.32$ m, and three different target initial solitary wave profiles were used with $\epsilon = 0.05$, 0.1 and 0.2. Solitary waves were generated using the procedure described by Synolakis (1987, 1990). Unfortunately, the digital-to-analog rate for the interface used in these experiments is only 20 Hz; solitary waves with as high a resolution as the solitary waves generated by Synolakis (i.e. whose digital-to-analog rate ranged from 1000 to 4000 Hz) were not generated. A typical command and feedback control signal for the paddle is shown in figure 6(*a*), where ξ represents the paddle movement. The corresponding free-surface displacements measured at gauge 1 (see figure 5), which is in front of the wave generator in the constant-depth region, is shown in figure 6(*b*).
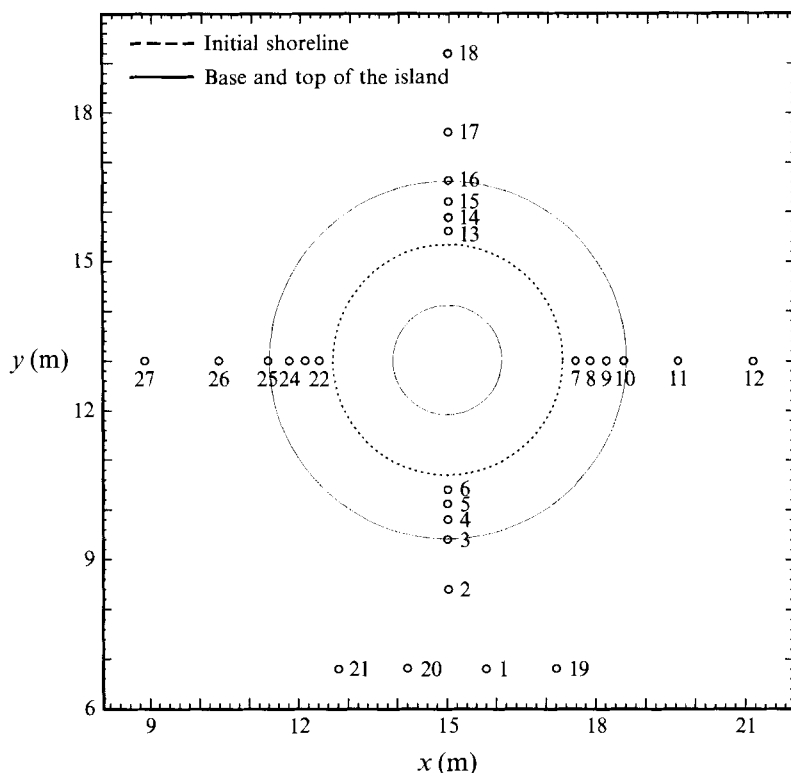
FIGURE 5. Locations of wave gauges.

Gauge	x (m)	y (m)	Gauge	x (m)	y (m)	Gauge	x (m)	y (m)
1	15.75	6.85	7	17.58	13.00	13	15.00	15.60
2	15.00	8.40	8	17.88	13.00	14	15.00	15.88
3	15.00	9.40	9	18.20	13.00	15	15.00	16.20
4	15.00	9.80	10	18.55	13.00	16	15.00	16.63
5	15.00	10.12	11	19.63	13.00	17	15.00	17.63
6	15.00	10.40	12	21.13	13.00	18	15.00	19.13

TABLE 1. Locations of wave gauges.

Module	Number of paddles	DSWG length L (m)	L/D
1	14	6.401	0.889
2	29	13.259	1.842
3	44	20.117	2.794
4	60	27.432	3.810

TABLE 2. Number of paddles and length of the DSWG.

Notice that the command and feedback signals are almost identical. These signals
were used directly in the numerical model to generate incident waves. In figure 6(b)
the dashed line represents the measured solitary wave profile, symmetric with respect
to the wave crest. Note however, that the calculated free-surface profile at gauge
1 shown by the solid line in figure 6(b) is more slanted and has a steeper front, a
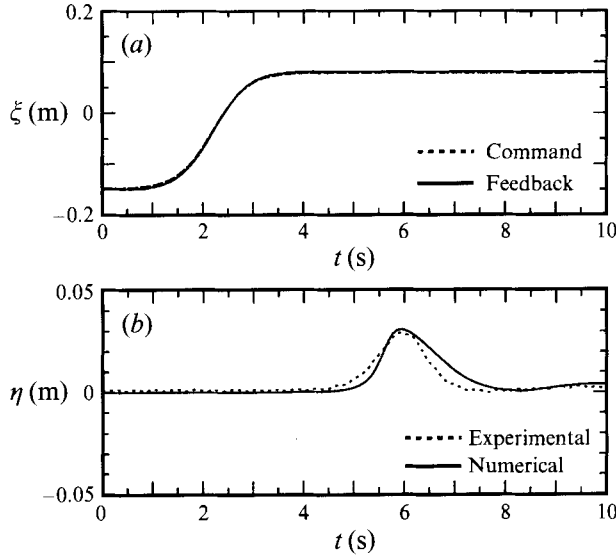result of using the shallow-water equations in the numerical experiments. Maximum

FIGURE 6. A typical command and feedback control signal for the paddle movement: (*a*) command and feedback control signal of the paddle; (*b*) time histories of free-surface displacement at wave gauge 1 ($\epsilon = 0.1, m = 4$).

runup heights were measured visually by standard surveying methods at 20 shoreline locations around the perimeter of the circular island. Sixteen locations were evenly spaced at $\pi/8$, and four were located symmetrically at $\pi/16$ around the lee side of the island to improve the resolution at that location.

Experimental data and observations will be discussed in §4. They will also be used to validate the numerical model presented in the following section.

3. Numerical model

The wavelength of the incoming tsunami is usually very long in comparison to the local water depth. Wave amplitude is also small in most of the flow domain, with the exception of a small region adjacent to the shoreline, where runup occurs. The frequency dispersion may become important if the travel distance of the tsunami is long. Kajiura (1963) suggested that if the travel distance R is shorter than $(a/h)^3(h/10)$, where a is the wave height and h the depth, frequency dispersion can be ignored. In the present problem, the maximum travel distance (the length of the basin) is 30 m, the depth is 0.320 m, and the typical wave height-to-depth ratio is 0.1. Therefore, the frequency dispersion is not important in most of the region near the island. In the present study, nonlinear shallow-water equations in the following form are used:

$$\frac{\partial \eta}{\partial t} + \frac{\partial P}{\partial x} + \frac{\partial Q}{\partial y} = 0, \tag{3.1}$$

$$\frac{\partial P}{\partial t} + \frac{\partial}{\partial x}\left(\frac{P^2}{H}\right) + \frac{\partial}{\partial y}\left(\frac{PQ}{H}\right) + gH\frac{\partial \eta}{\partial x} = 0, \tag{3.2}$$

$$\frac{\partial Q}{\partial t} + \frac{\partial}{\partial x}\left(\frac{PQ}{H}\right) + \frac{\partial}{\partial y}\left(\frac{Q^2}{H}\right) + gH\frac{\partial \eta}{\partial y} = 0, \tag{3.3}$$

where η denotes the free-surface displacement, $H = \eta + h$ is the total water depth, and h is the still-water depth. P and Q are the horizontal components of the volume flux in the x- and y-directions, respectively. In the event that bottom frictional effects become important, the bottom friction can be modelled by Manning's formula, i.e. frictional terms in the form of

$$\frac{gn^2}{H^{7/3}} \, P \, (P^2 + Q^2)^{1/2} \quad \text{and} \quad \frac{gn^2}{H^{7/3}} \, Q \, (P^2 + Q^2)^{1/2}$$

are introduced in the momentum equations (3.2) and (3.3), respectively. In the above expressions, n is the Manning's relative roughness coefficient.

A staggered explicit finite difference leap-frog scheme is used to solve governing equations (3.1)–(3.3). Nonlinear convective terms are linearized with an upwind scheme. Finite difference formulas for the numerical scheme are given in Appendix A. In modelling the circular island experiments, only one half of the basin (15 $\leqslant x \leqslant$ 30 m, 0 $\leqslant y \leqslant$ 25 m, see figure 4) including one half of the circular island, was used as the computational domain because of the symmetry. Along the wave generator, the y-component of the volume flux Q is described. Along the centreline of the wave basin ($x = 15$ m, $0 \leqslant y \leqslant 25$ m), the x-component of the volume flux P vanishes. A radiation boundary condition based on the method of characteristics is applied along the other two boundaries (15 $\leqslant x \leqslant$ 30 m, $y = 25$ m; and $x = 30$ m, $0 \leqslant y \leqslant 25$ m) as well as the wave generator, so that outward-going waves propagate through these boundaries without significant reflection.

In the numerical computations, the computational domain is divided into a finite number of cells. Initially, the free-surface displacement is zero everywhere, as are the volume fluxes. When the grid point is on dry land, the 'water depth' h takes a negative value and gives the elevation of the land measured from the mean water level. The interface between the dry cell and the wet cell defines the shoreline, where the water depth is zero. A numerical algorithm is employed in conjunction with the leap-frog method to track shoreline movement. Similar algorithms for the moving shoreline can be found in Aida (1977), Houston & Butler (1979), and Hibberd & Peregrine (1979). Descriptions of the radiation boundary condition and the moving boundary algorithm used in the present paper are given in Appendix B. In the numerical experiments, friction was not found to be important. For example, by assuming a Manning's coefficient $n = 0.013$ (the proper value for smooth concrete (Chow 1959)) then for a 0.1 incident wave height-to-depth ratio and four-module wavemaker, runup varied by only 0.5% as compared with the value with no friction. Therefore, in the subsequent calculations the friction terms are not included, which may be of importance in specific field problems.

Numerical simulations of the laboratory experiments have been performed for all cases (Cho 1994). Only a small set of results will be discussed in detail in this paper. To facilitate discussion of the results in the following sections, a sequence of snapshot-type figures of free-surface displacement of an $\epsilon = 0.1$ wave in the vicinity of the circular island is first presented. In the numerical computations, mesh size and time-step size were fixed, $\Delta x = \Delta y = 0.1$ m and $\Delta t = 0.02$ s. As shown in figure 7(a–c), the incident solitary wave attacks the front end of the island and generates significant runup. Once the wave reaches its maximum runup heights along the front of the island, the wave runs down the beach back to the waterline and creates a cylindrical wave pattern. A portion of the wave propagates along the shoreline towards the lee side of the island (see figure 7c, $t = 11$ s). Because of the island bathymetry, the
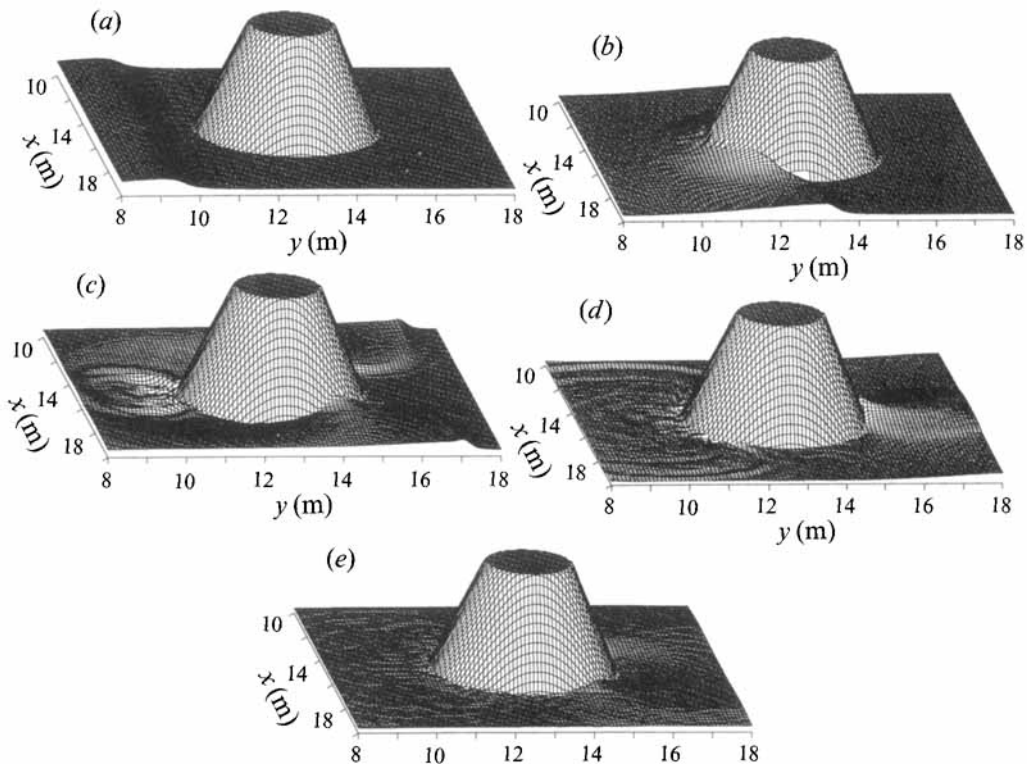
FIGURE 7. Snapshots of free-surface profiles at different times ($\epsilon = 0.1$, module 4): (*a*) $t = 7$ s, a solitary wave approaches the island; (*b*) $t = 9$ s, wave runup occurs in the front of the island; (*c*) $t = 11$ s, three-dimensional waves appear in the front of the island and the trapped wave propagates along the shoreline; (*d*) $t = 13$ s, two trapped waves collide in the lee side of the island; (*e*) $t = 15$ s, trapped waves propagate continuously along the shore after the collision.

crest line of the leading wave is bent, i.e. the wave form propagates with a faster speed offshore because of greater depth. In figure 7(*c*), the wave crest line indicates that while the solitary wave propagates in the *y*-direction far offshore, waves on the island shoal are propagating in alongshore directions at a slower speed. The latter have a large amplitude at the shoreline, which decays exponentially offshore in the radial direction. These two wave components, the incident solitary wave and the trapped wave propagating around the island, are eventually separated at $t = 13$ s (see figure 7*d*, where the solitary wave has moved out of the picture). At this moment, two trapped waves collide with each other in the lee side of the island and generate high runup heights. These trapped waves pass through each other and continue propagating around the island in figure 7(*e*). Because they are not perfectly trapped, waves and certain amounts of energy are leaking continuously into offshore areas. Then these trapped waves die out gradually. These features are similar to those demonstrated by the ray theory (see figure 3*b*), i.e. the rays near the centreline impinge on the front side of the island, while the rays far away from the centreline whirl around the island before reaching the shore. However, the present solutions include nonlinear effects, diffraction effects, and the effect of a moving shoreline.
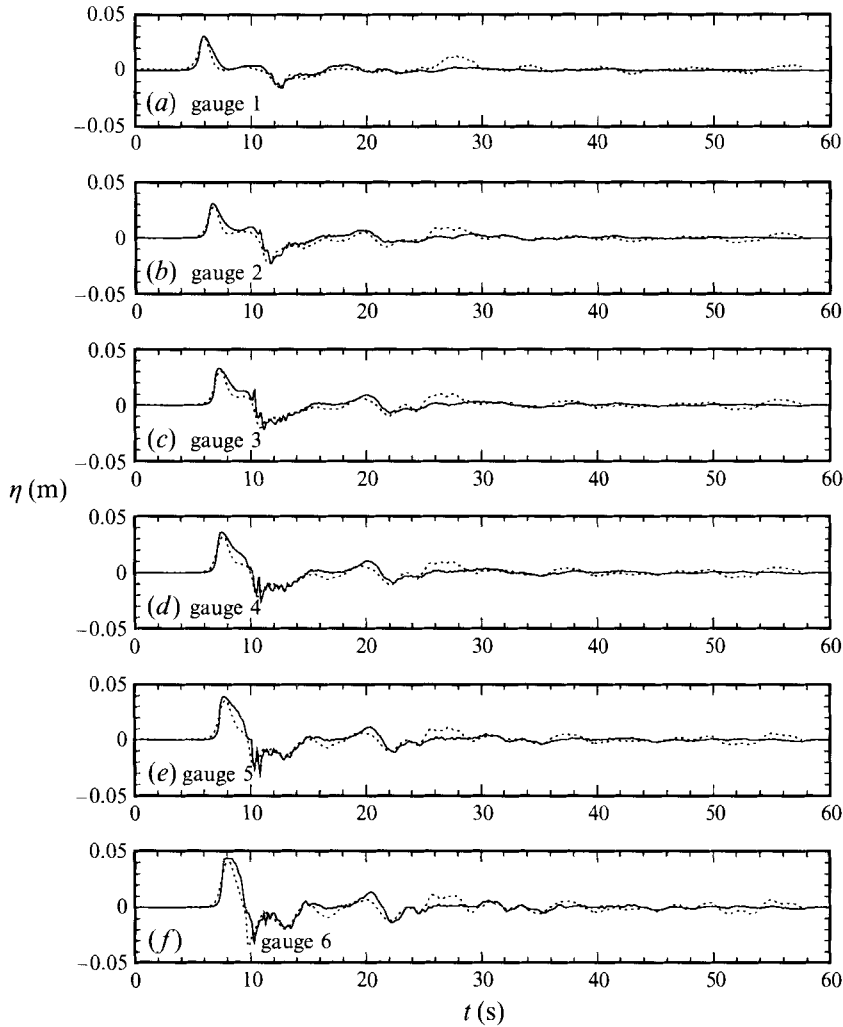
η (m)

t (s)

FIGURE 8 (a–f). For caption see page 270.

4. Comparisons between laboratory experiments and numerical simulations

This section presents only a small portion of detailed comparisons between laboratory and numerical experiments. More comparisons with numerical results are presented in Cho (1994) and with analytical results in Kanoglu (1995).

4.1. Free-surface displacement

Figure 8 presents comparisons between wave gauge data and numerical results for an $\epsilon = 0.1$ incident solitary wave and where the length of the wave generator is 27.432 m (module 4 in table 2). Locations of the wave gauges are shown in table 1 and in figure 5. Overall agreement between numerical solutions and experimental data is good and the numerical-generated free-surface profiles of the leading wave have steeper fronts, as noted earlier in figure 6(b). This is a typical feature of the shallow-water equation solutions. Nevertheless, wave height and total volume are the same in both the numerical results and the experimental data. In front of the island, wave gauges 1–6 show a leading wave followed by a depression wave, resembling the
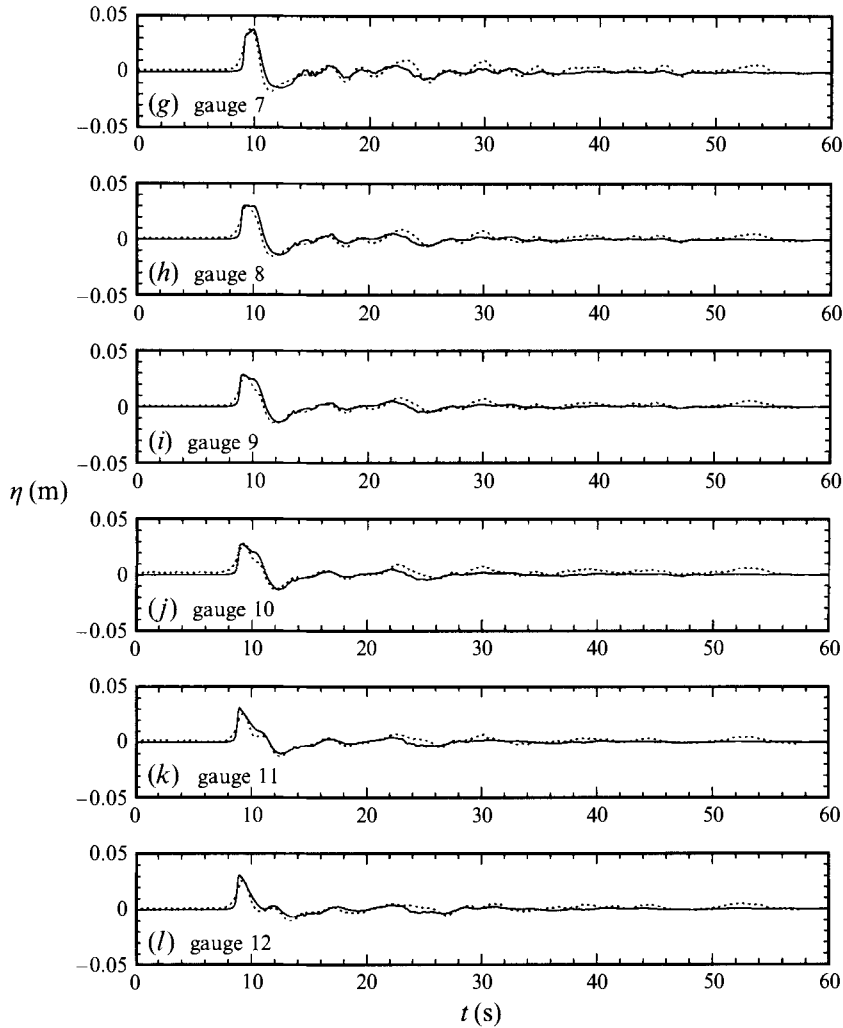
FIGURE 8(*g–l*) For caption see page 270.

LEN waves of Tadepalli & Synolakis (1994). However, the depression wave here is the reflected wave from the island slope in Carrier & Noiseux (1983) and Synolakis (1987). The reflected nature of this wave was also confirmed by calculating the travel time of the depression wave from gauge 3 to gauge 1. The distance in the y-direction between these two gauges is 2.55 m. The numerical wave height of the depression wave at gauge 3 was estimated as -0.02 m, its phase speed as 1.72 ms^{-1}, and its travel time for the depression wave from gauge 3 to gauge 1 as 1.49 s, almost exactly the same to that estimated from experimental data. Note that the second elevation wave appears in the experimental data, which can not be reproduced in the numerical solutions. This second elevation wave is the re-reflected wave from the wave generator. In the numerical model a radiation boundary condition has been employed so that the reflected wave from the island propagates out of the computational domain without being re-reflected. On the lee side of the island the reflection of the solitary waves from the boundary of the basin is also evident (figure 8*m–r*). Once again, numerical results do not reproduce these reflected waves, because of the radiation boundary condition.
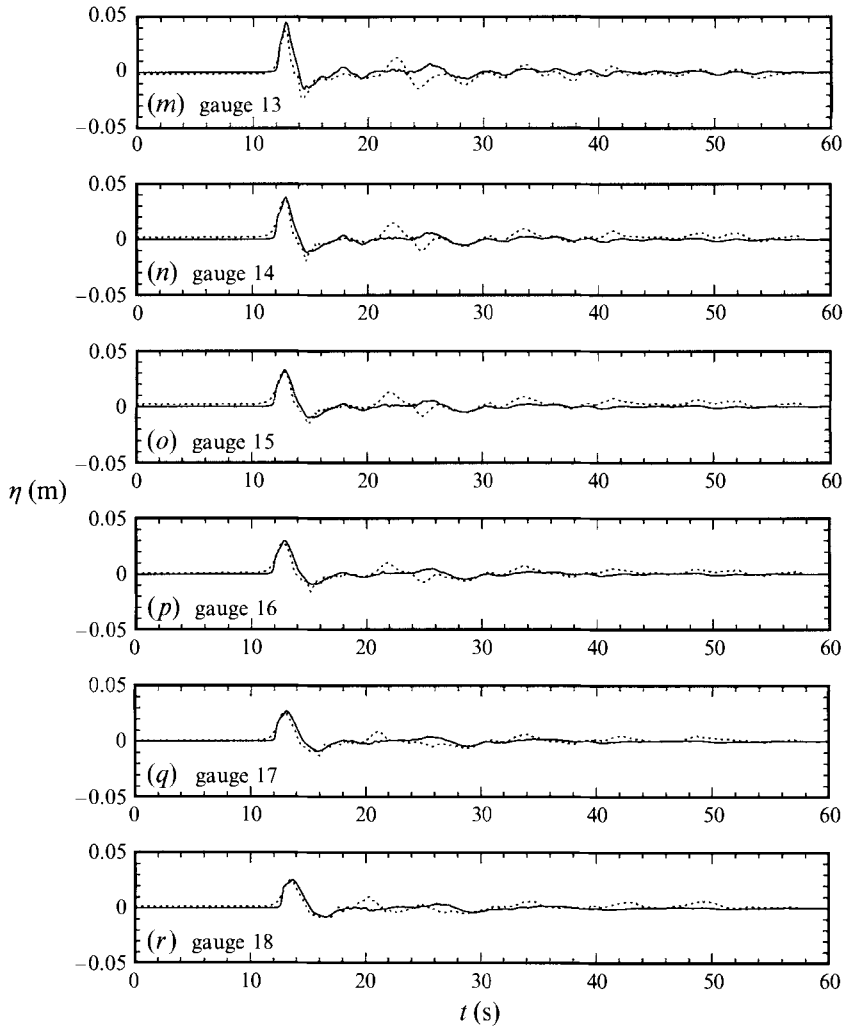
FIGURE 8. Time histories of free-surface displacements ($\epsilon = 0.1$, module 4) at different wave gauge locations: ······, experimental data; ———, numerical solutions.

However, these re-reflected waves do not affect the maximum runup heights observed in the laboratory; the maximum runup observed was always due to the first wave, and subsequent reflections produced significantly smaller runup values.

As demonstrated in figure 7, because of refraction the crest line of the leading wave bends towards the direction perpendicular to the shoreline except in the region very near the shore. This feature is further illustrated by plotting the arrival time of the leading wave crest along wave gauges 7–12 and 13–18, respectively. Arrival times are of engineering importance in the deployment of tsunami warning systems, and therefore accurate predictions are a significant validation test for any tsunami inundation model. In figure 9(a), arrival times obtained from the experimental data and numerical solutions for gauges 7–12 are plotted, all parallel to the wave generator. Arrival times at offshore gauges 11 and 12 are almost identical and shorter than those on the island slope. Arrival times vary almost linearly on the slope, with the longest time at the shallowest water. In the lee of the island at wave gauges 13–18, this trend
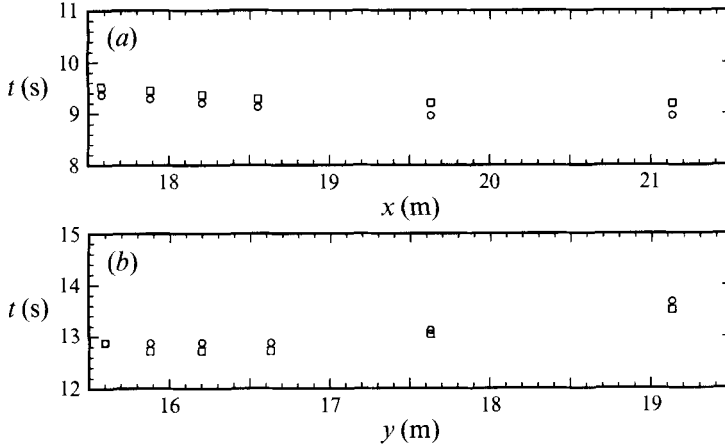
FIGURE 9. Arrival times of the leading wave crest ($\epsilon = 0.1$, module 4) along two cross-sections (*a*) $\beta = \pi/2$, gauges 7–12 and (*b*) $\beta = \pi$, gauges 13–18: □, experimental data; ○, numerical solutions.
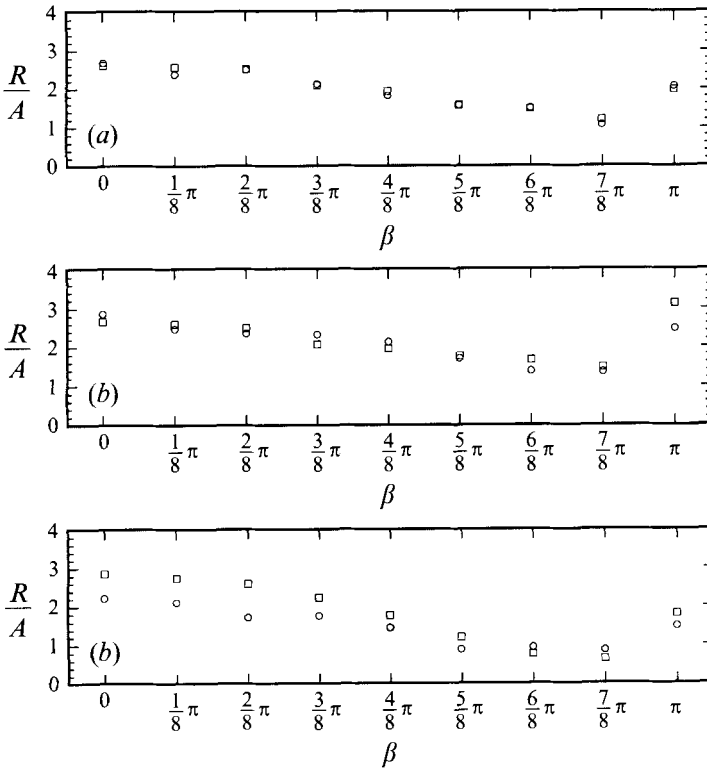

FIGURE 10. Comparisons of the normalized runup height distribution around the island: (*a*) $\epsilon = 0.05$, (*b*) $\epsilon = 0.1$, (*c*) $\epsilon = 0.2$: □, experimental data; ○, numerical solutions.

of arrival times is reversed and is shown in figure 9(*b*). These arrival times are longer in the offshore region than those on the slope and are caused by the bending of the leading wave crest line. Furthermore, arrival times of the wave crest on the slope are almost identical, indicating that the crest line is nearly parallel to the shoreline.
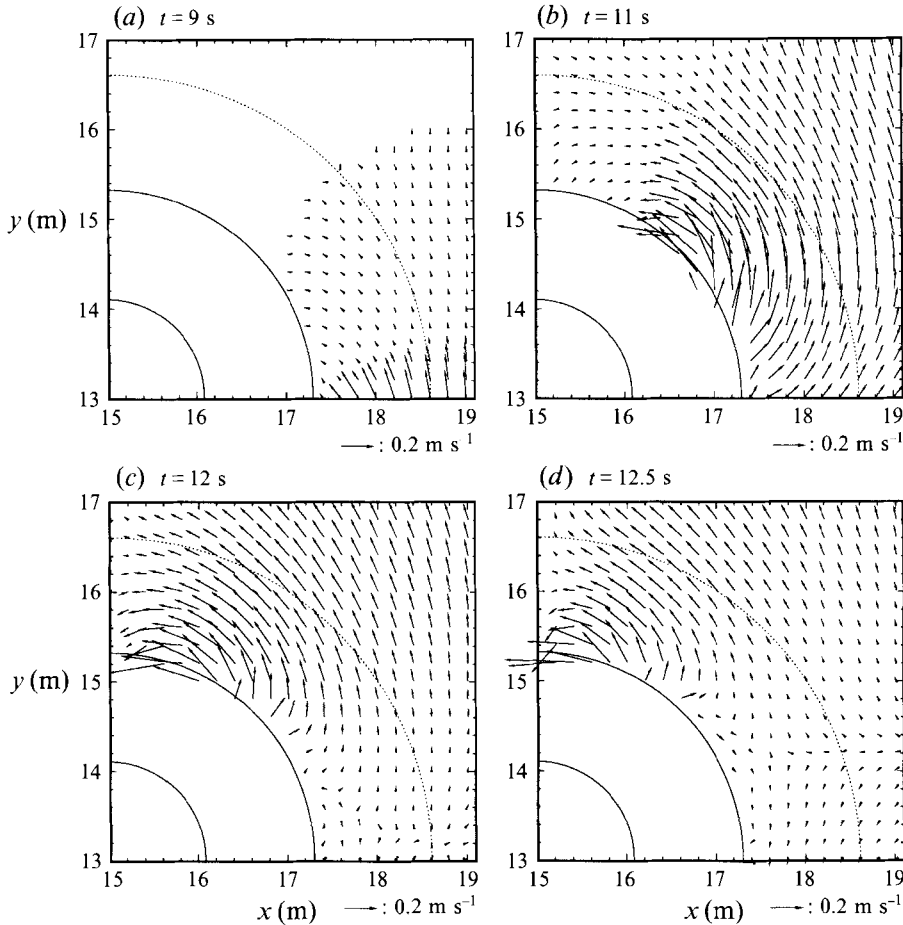
FIGURE 11. Snapshots of velocity distribution at different times ($\epsilon = 0.1$, module 4) at the back of the island, $\pi/2 < \beta < \pi$.

4.2. *Maximum runup heights*

In figure 10, normalized maximum runup heights around the island are presented for different incident wave heights; here the angle β is measured in the counterclockwise direction around the island from the incoming wave direction. For the cases where wave heights are 0.032 m ($\epsilon = 0.1$) and 0.016 m ($\epsilon = 0.05$), normalized maximum runup heights are almost identical. Large differences were observed between the numerical results and the laboratory data when the incident wave height was 0.064 m ($\epsilon = 0.2$). This is when the wave broke in its laboratory realization, and a non-breaking wave model is used in the numerical computations. To our knowledge, no numerical solution has been demonstrated to successfully reproduce breaking in a two-dimensional flow and this remains an important but unsolved question.

In general, maximum runup height is largest in front of the island (i.e. $\beta = 0$) and it decreases gradually as the wave moves toward the lee side of the island at $\beta = \pi$. If the length of the wave generator is much larger than the base diameter of the island (e.g. for the module 4 case), there is a drastic increase in maximum runup height at the lee of the island, see for example the $\beta = \pi$ case in figure 10. This is because of the collision of the two trapped waves shown in figure 7(d). When $\epsilon = 0.1$, the
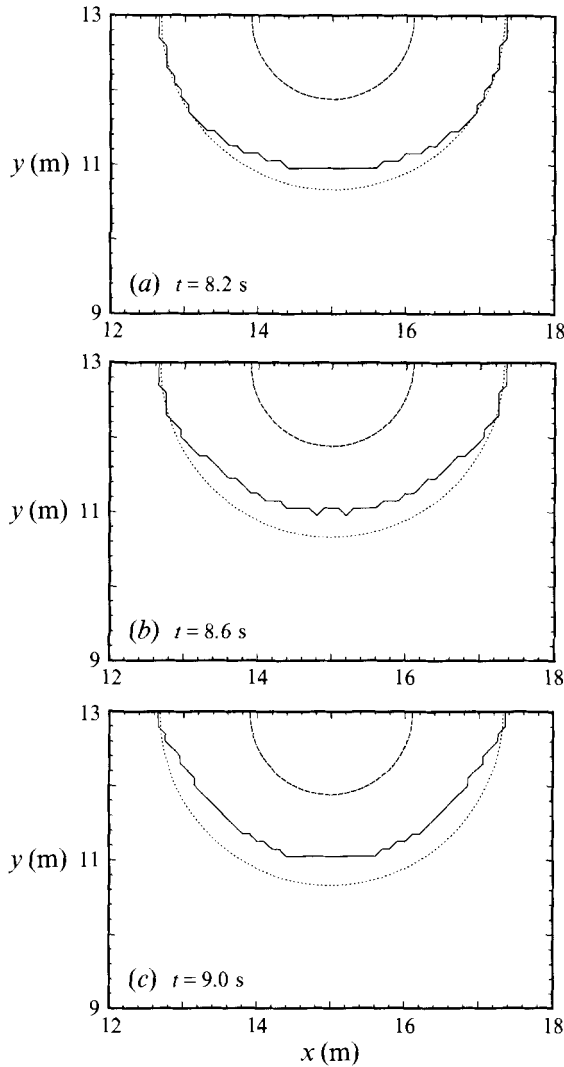
FIGURE 12. Instantaneous shoreline locations in front of the island near the maximum runup height ($t = 9.0$ s) for $\epsilon = 0.1$ and module 4: ······, initial shoreline; - - - -, the top of the island; ——, shoreline location.

maximum runup height at $\beta = \pi$ is actually larger than that measured at the front $\beta = 0$. However, the numerical model did not reproduce this feature. This enhanced runup height in the lee side of the island will be discussed in greater detail in the following section.

5. Discussion

This section will describe results of the numerical model not readily available from the experimental data. The model will also be extended to study other ranges of the physical parameters, to further elucidate the runup patterns around the island.

The numerical model calculates the volume flux components P and Q at each time step. These can be converted to the depth-averaged velocity vector. Figure 11
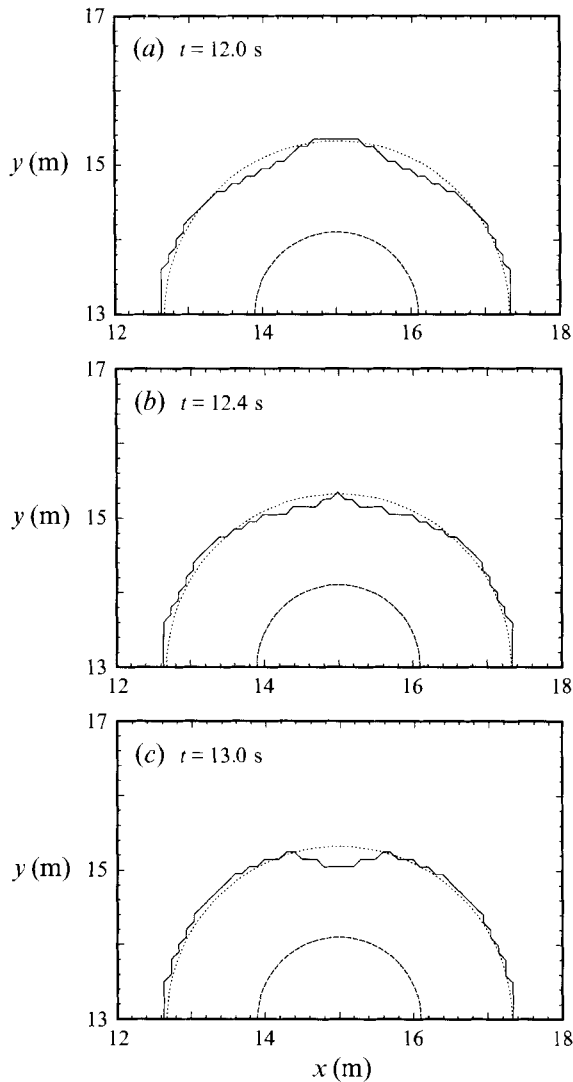
FIGURE 13. Instantaneous shoreline locations in the lee of the island near the maximum runup height ($t = 13.2$ s) for $\epsilon = 0.1$ and module 4: · · · · · ·, initial shoreline; - - - -, the top of the island; ———, shoreline location.

shows a sequence of snapshots of velocity distributions at the back of the island, $\pi/2 < \beta < \pi$, for $\epsilon = 0.1$ and module 4. Owing to symmetry, velocity patterns in the region $\pi < \beta < 3\pi/2$ are mirror images of those shown in figure 11. Corresponding free-surface displacements are shown in figure 7. It is evident that although wave celerity is smaller near the shoreline, the depth-averaged particle velocity is much larger near the shoreline. Two trapped waves collide at the lee side of the island and create the maximum particle velocity at $t = 12.5$ s.

The affected area during the runup in front of the island is much wider than that in the lee of the island. In figure 12, a sequence of shoreline locations in front of the island before the runup height reaches its maximum is shown. At maximum runup (i.e. $t = 9$ s) almost the entire front half of the island is inundated, yet the runup in the lee of the island floods a much smaller area (see figure 13).
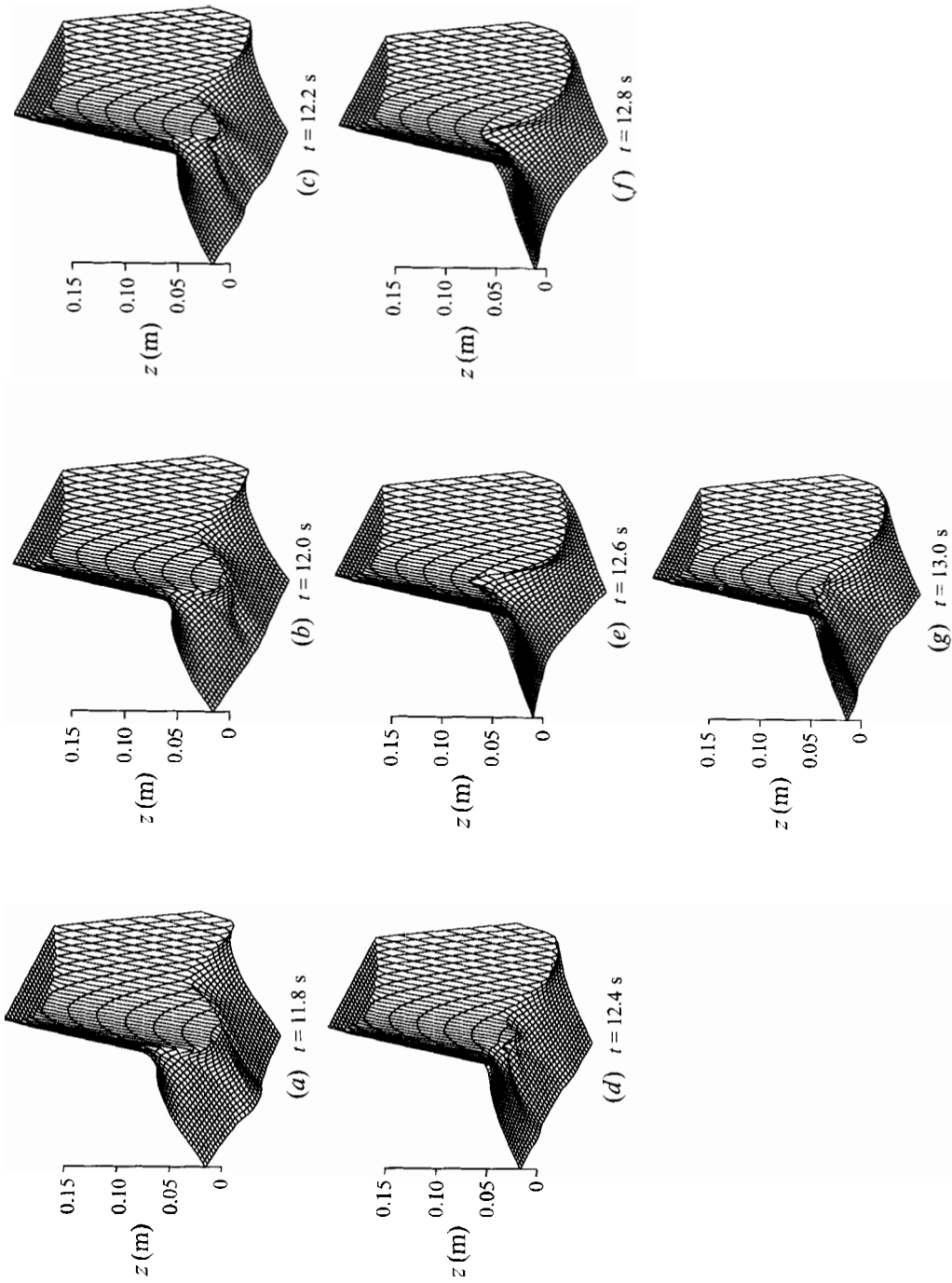
FIGURE 14. Free-surface configurations in the lee of the island.

The difference can be explained as follows: during the runup phase, the velocity field in front of the island is mostly in the onshore direction over a relatively broad area. On the other hand, in the lee of the island, the velocities are in the alongshore direction before the trapped waves collide with each other (see figure 11c–d). Because of the symmetry and because the shoreline is allowed to move, alongshore velocities near the shoreline turn into the onshore direction very sharply at the time of collision. This causes the enhanced and focused runup area in the lee of the island.

To illustrate the dynamics of the enhanced runup, a sequence of the free-surface configurations in the lee of the island is shown in figure 14. At $t = 11.8$ s, two leading waves almost reach the line of symmetry. Wave crests in the deeper water move faster than those along the shoreline at $t = 12$ s. The two wave crests meet offshore first, as shown in figure 14(b); their collision produces a surge towards the shore, while the wave crests along the shoreline approach each other continuously (see figure 14c,d). Once the wave crests along the shoreline collide into each other, shoreward surging is enhanced. The maximum runup height along the symmetry line is reached at $t = 13$ s.

Figure 15 presents amplitude variations in the on-offshore direction at two different locations ($\beta = \pi/2$ and π) over two different time periods. The beginning of each period represents the moment when the wave starts to run down the beach. In the figure, the profile for the Stokes mode edge wave on a plane beach is also plotted. The Stokes mode edge wave is assumed to have the same wave period as that of the incident solitary wave, which is estimated from the duration of the wave-maker motion (Briggs, Synolakis & Harkins 1994). From the present experiments, the wave period of the incoming solitary wave is calculated as 4.905 s when the wave height is 0.032 m and the offshore water depth is 0.32 m. From the linear shallow-water theory, the free-surface profile of the Stokes mode edge wave on a plane sloping beach is given by (Schäffer & Jonsson 1992)

$$\eta = A_\circ \exp\left(-\mu\psi\right)\cos\left(\mu\chi - \omega t\right) \tag{5.1}$$

in which the wavenumber of the Stokes mode edge wave μ is given by

$$\mu = \frac{\omega^2}{g\tan\theta} \tag{5.2}$$

with ω and θ being the angular frequency and the beach angle, respectively. Using $\theta = 14.04°$ and $T = 4.905$ s, μ is calculated as 0.669. $A_\circ$ denotes the shoreline amplitude and (χ, ψ) represent Cartesian coordinates with the origin at the shoreline; the χ-axis points in a counterclockwise direction and the ψ-axis points in the seaward direction, respectively. In figure 15, the measured shoreline amplitude at the beginning of each period is used as $A_\circ$ in (5.1). It is very clear that the calculated trapped waves leak wave energy in the seaward direction and cannot be fully described by the Stokes mode edge wave.

Finally, the effects of beach slope on runup heights of the circular island were investigated. Figure 16 compares the normalized maximum runup heights for an $\epsilon = 0.1$ wave for three different beach slopes ($\theta = 14.04°$, 20° and 30°). Similar to the two-dimensional plane beach cases (Liu & Cho 1994), the maximum runup height decreases as beach slope increases. The variation of runup heights around the island remains similar in all three cases.
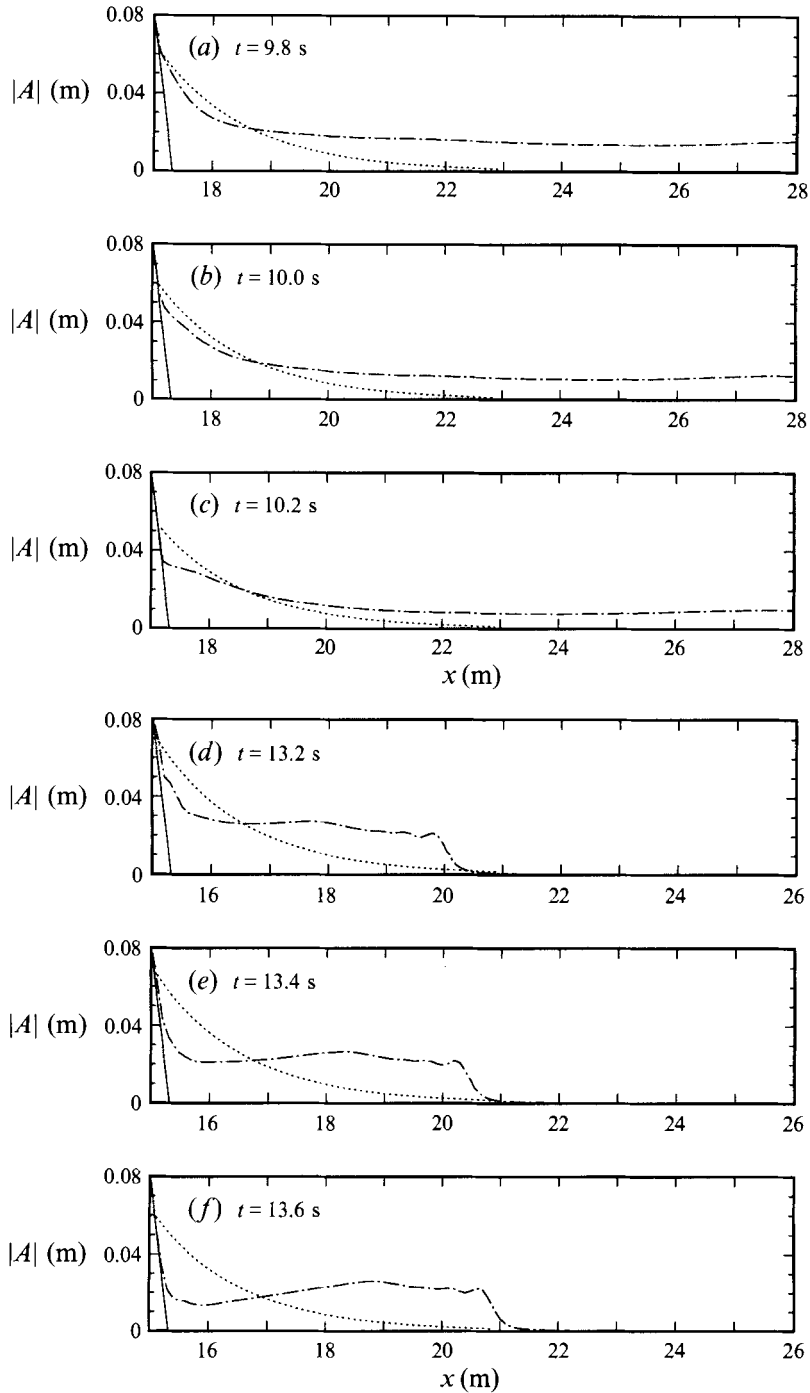
FIGURE 15. Comparisons between the calculated profiles of free-surface elevations in the on-offshore direction and the Stokes mode edge waves: (a)–(c) $\beta = \pi/2$, (d)–(f) $\beta = \pi$. $\cdots\cdots$, Stokes mode edge waves; — · — ·, numerical results.

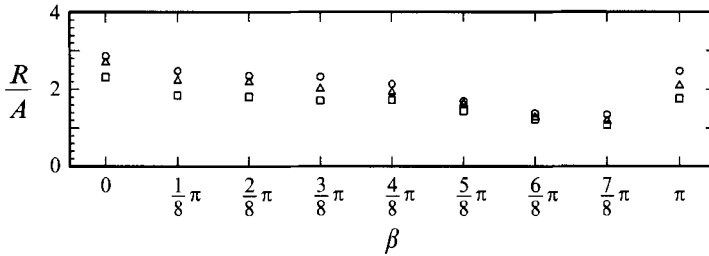FIGURE 16. Maximum runup heights around the island for different island slope:
$\circ$, $\theta = 14.04°$; $\triangle$, $\theta = 20°$; $\square$, $\theta = 30°$.

6. Conclusions

A series of laboratory experiments and a new model for studying the evolution and runup of a solitary wave around a circular island have been presented. When the laboratory manifestation of the wave does not break on the front of the island, good agreement between laboratory data and numerical results has been founded. Based on the findings of this study, it can be concluded that the solitary wave runup around a circular island may produce enhanced runup of the lee side of the island, depending primarily on the ratio of the crest length of the wave to the island diameter. Maximum runup decreases as beach slope increases. These results help explain the mechanism of the catastrophe on Babi island, where unusually large inundation was observed on the lee side of the island. Numerical solutions for the depth-averaged velocity distributions indicate that the velocity tends to be strong nearshore and could cause significant sediment transport if the island has a sandy beach.

Appendix A

This appendix presents finite difference forms for the nonlinear shallow-water equations, (3.1)–(3.3). The governing equations without nonlinear terms can be discretized with the staggered explicit leap-frog finite difference scheme as

$$\frac{\eta_{i,j}^{n+1/2} - \eta_{i,j}^{n-1/2}}{\Delta t} + \frac{P_{i+1/2,j}^{n} - P_{i-1/2,j}^{n}}{\Delta x} + \frac{Q_{i,j+1/2}^{n} - Q_{i,j-1/2}^{n}}{\Delta y} = 0, \tag{A 1}$$

$$\frac{P_{i+1/2,j}^{n+1} - P_{i+1/2,j}^{n}}{\Delta t} + gH_{i+1/2,j}^{n+1/2} \frac{\eta_{i+1,j}^{n+1/2} - \eta_{i,j}^{n+1/2}}{\Delta x} = 0, \tag{A 2}$$

$$\frac{Q_{i,j+1/2}^{n+1} - Q_{i,j+1/2}^{n}}{\Delta t} + gH_{i,j+1/2}^{n+1/2} \frac{\eta_{i,j+1}^{n+1/2} - \eta_{i,j}^{n+1/2}}{\Delta y} = 0. \tag{A 3}$$
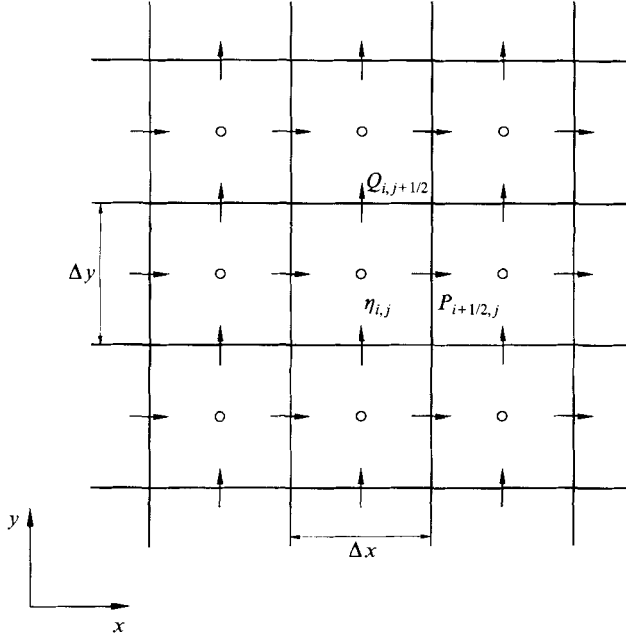
FIGURE 17. Staggered finite difference grid system.

As shown in figure 17, the index (i, j) denotes spatial nodes and n represents time level. Free-surface displacement and water depth are defined at the centre of each grid cell, while volume fluxes are defined at the interfaces of the grid. Δx and Δy represent the spatial step sizes in the x- and the y-directions, respectively, and Δt stands for the time-step size. Nonlinear convective terms are discretized with the upwind scheme. Thus, the nonlinear terms of the momentum equations are discretized as

$$\frac{\partial}{\partial x}\left(\frac{P^2}{H}\right) = \frac{1}{\Delta x}\left[\lambda_{11}\frac{\left(P_{i+3/2,j}^n\right)^2}{H_{i+3/2,j}^n} + \lambda_{12}\frac{\left(P_{i+1/2,j}^n\right)^2}{H_{i+1/2,j}^n} + \lambda_{13}\frac{\left(P_{i-1/2,j}^n\right)^2}{H_{i-1/2,j}^n}\right], \quad (A\,4)$$

$$\frac{\partial}{\partial y}\left(\frac{PQ}{H}\right) = \frac{1}{\Delta y}\left[\lambda_{21}\frac{(PQ)_{i+1/2,j+1}^n}{H_{i+1/2,j+1}^n} + \lambda_{22}\frac{(PQ)_{i+1/2,j}^n}{H_{i+1/2,j}^n} + \lambda_{23}\frac{(PQ)_{i+1/2,j-1}^n}{H_{i+1/2,j-1}^n}\right], \quad (A\,5)$$

$$\frac{\partial}{\partial x}\left(\frac{PQ}{H}\right) = \frac{1}{\Delta x}\left[\lambda_{31}\frac{(PQ)_{i+1,j+1/2}^n}{H_{i+1,j+1/2}^n} + \lambda_{32}\frac{(PQ)_{i,j+1/2}^n}{H_{i,j+1/2}^n} + \lambda_{33}\frac{(PQ)_{i-1,j+1/2}^n}{H_{i-1,j+1/2}^n}\right], \quad (A\,6)$$

$$\frac{\partial}{\partial y}\left(\frac{Q^2}{H}\right) = \frac{1}{\Delta y}\left[\lambda_{41}\frac{\left(Q_{i,j+3/2}^n\right)^2}{H_{i,j+3/2}^n} + \lambda_{42}\frac{\left(Q_{i,j+1/2}^n\right)^2}{H_{i,j+1/2}^n} + \lambda_{43}\frac{\left(Q_{i,j-1/2}^n\right)^2}{H_{i,j-1/2}^n}\right]. \quad (A\,7)$$

where the coefficients, λ, are determined from

$$\lambda_{11} = 0, \quad \lambda_{12} = 1, \quad \lambda_{13} = -1, \quad \text{if } P_{i+1/2,j}^n \geqslant 0$$
$$\lambda_{11} = 1, \quad \lambda_{12} = -1, \quad \lambda_{13} = 0, \quad \text{if } P_{i+1/2,j}^n < 0,$$

$$\lambda_{31} = 0, \quad \lambda_{32} = 1, \quad \lambda_{33} = -1, \quad \text{if } P^n_{i,j+1/2} \geqslant 0$$
$$\lambda_{31} = 1, \quad \lambda_{32} = -1, \quad \lambda_{33} = 0, \quad \text{if } P^n_{i,j+1/2} < 0,$$

$$\lambda_{41} = 0, \quad \lambda_{42} = 1, \quad \lambda_{43} = -1, \quad \text{if } Q^n_{i,j+1/2} \geqslant 0$$
$$\lambda_{41} = 1, \quad \lambda_{42} = -1, \quad \lambda_{43} = 0, \quad \text{if } Q^n_{i,j+1/2} < 0.$$

Since the upwind scheme is employed, it should be reiterated that the discretized momentum equations are only first order in accuracy in terms of spatial grid sizes. Finally, the finite difference equations for the continuity and momentum equations can be written as

$$\eta^{n+1/2}_{i,j} = \eta^{n-1/2}_{i,j} - r_x\left(P^n_{i+1/2,j} - P^n_{i-1/2,j}\right) - r_y\left(Q^n_{i,j+1/2} - Q^n_{i,j-1/2}\right), \tag{A 8}$$

$$P^{n+1}_{i+1/2,j} = \left[P^n_{i+1/2,j} - r_x g H^{n+1/2}_{i+1/2,j}\left(\eta^{n+1/2}_{i+1,j} - \eta^{n+1/2}_{i,j}\right)\right]$$
$$-r_x\left[\lambda_{11}\frac{\left(P^n_{i+3/2,j}\right)^2}{H^n_{i+3/2,j}} + \lambda_{12}\frac{\left(P^n_{i+1/2,j}\right)^2}{H^n_{i+1/2,j}} + \lambda_{13}\frac{\left(P^n_{i-1/2,j}\right)^2}{H^n_{i-1/2,j}}\right]$$
$$-r_y\left[\lambda_{21}\frac{(PQ)^n_{i+1/2,j+1}}{H^n_{i+1/2,j+1}} + \lambda_{22}\frac{(PQ)^n_{i+1/2,j}}{H^n_{i+1/2,j}} + \lambda_{23}\frac{(PQ)^n_{i+1/2,j-1}}{H^n_{i+1/2,j-1}}\right], \tag{A 9}$$

$$Q^{n+1}_{i,j+1/2} = \left[Q^n_{i,j+1/2} - r_y g H^{n+1/2}_{i,j+1/2}\left(\eta^{n+1/2}_{i,j+1} - \eta^{n+1/2}_{i,j}\right)\right]$$
$$-r_x\left[\lambda_{31}\frac{(PQ)^n_{i+1,j+1/2}}{H^n_{i+1,j+1/2}} + \lambda_{32}\frac{(PQ)^n_{i,j+1/2}}{H^n_{i,j+1/2}} + \lambda_{33}\frac{(PQ)^n_{i-1,j+1/2}}{H^n_{i-1,j+1/2}}\right]$$
$$-r_y\left[\lambda_{41}\frac{\left(Q^n_{i,j+3/2}\right)^2}{H^n_{i,j+3/2}} + \lambda_{42}\frac{\left(Q^n_{i,j+1/2}\right)^2}{H^n_{i,j+1/2}} + \lambda_{43}\frac{\left(Q^n_{i,j-1/2}\right)^2}{H^n_{i,j-1/2}}\right], \tag{A 10}$$

in which

$$r_x = \frac{\Delta t}{\Delta x}, \quad r_y = \frac{\Delta t}{\Delta y}.$$

The following approximations have been used to derive finite difference equations (A 8)–(A 10):

$$H^{n+1/2}_{i+1/2,j} = \tfrac{1}{2}\left(H^{n+1/2}_{i,j} + H^{n+1/2}_{i+1,j}\right), \tag{A 11}$$

$$H^{n+1/2}_{i,j+1/2} = \tfrac{1}{2}\left(H^{n+1/2}_{i,j} + H^{n+1/2}_{i,j+1}\right), \tag{A 12}$$

$$H^n_{i+1/2,j} = \tfrac{1}{4}\left(H^{n-1/2}_{i,j} + H^{n+1/2}_{i,j} + H^{n-1/2}_{i+1,j} + H^{n+1/2}_{i+1,j}\right), \tag{A 13}$$

$$H^n_{i,j+1/2} = \tfrac{1}{4}\left(H^{n-1/2}_{i,j} + H^{n+1/2}_{i,j} + H^{n-1/2}_{i,j+1} + H^{n+1/2}_{i,j+1}\right), \tag{A 14}$$

$$P^n_{i,j+1/2} = \tfrac{1}{4}\left(P^n_{i-1/2,j} + P^n_{i-1/2,j+1} + P^n_{i+1/2,j} + P^n_{i+1/2,j+1}\right), \tag{A 15}$$

$$Q^n_{i+1/2,j} = \tfrac{1}{4}\left(Q^n_{i,j-1/2} + Q^n_{i+1,j-1/2} + Q^n_{i,j+1/2} + Q^n_{i+1,j+1/2}\right). \tag{A 16}$$
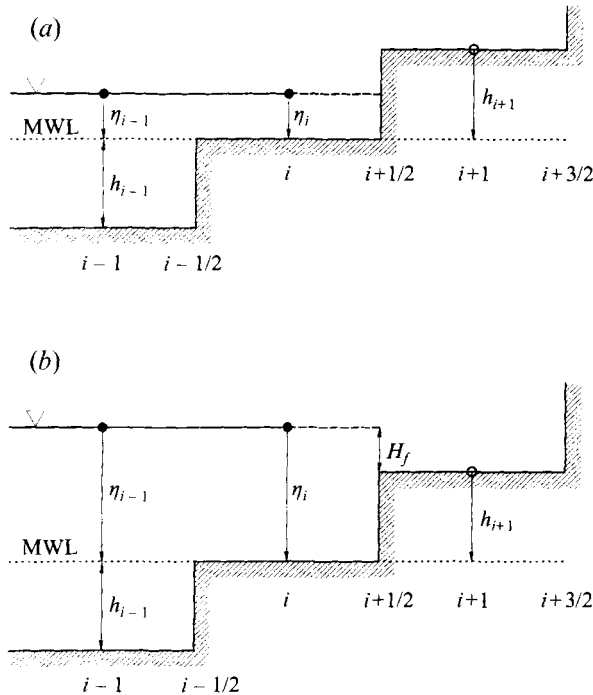
FIGURE 18. Moving boundary treatment: (*a*) case 1; (*b*) case 2.

Appendix B

This appendix describes the moving boundary and radiation boundary conditions imposed along the shoreline and the outer boundaries, respectively.

B.1. *Moving boundary condition*

Initial conditions for the present problem require that free-surface displacement and volume fluxes be zero everywhere in the computational domain. When the grid point is on dry land, the 'water depth' h takes a negative value and gives the elevation of the land measured from the mean water level. In a land (dry) cell the total depth $H = h + \eta$ has a negative value. On the other hand, the wet cell has a positive H value. The interface between the dry cells and wet cells defines the shoreline. Figure 18 shows a schematic sketch of the moving boundary treatment used in the study. MWL represents the still-water depth and H_f denotes the flooding depth. The continuity equation, in conjunction with boundary conditions along offshore boundaries, is used to find free-surface displacements at the next time step in the entire computational domain, including the dry (land) cells. The free-surface displacement at a dry land grid remains zero, because the volume fluxes are zero at the neighbouring grid points (see figure 17). At a shoreline grid, the total depth H is updated. A numerical algorithm is needed to determine if the shoreline should be moved. Momentum equations are used to update the volume fluxes in the wet cells only.

To illustrate the numerical algorithm for the moving boundary, the one-dimensional case is used as an example. As shown in figure 18, real bathymetry has been replaced by a staircase representation. Total depths H are calculated and recorded at $i-1$, i, and $i+1$ grid points, while volume fluxes are computed at $i-1/2$, $i+1/2$, and $i+3/2$ grid points. As shown in figure 18(*a*) the *i*th cell is a wet cell in which the total depth is positive and the $(i+1)$th cell is a dry (land) cell with a negative total depth. The

volume flux at the $i+3/2$ grid point is zero. The shoreline is somewhere between the ith and the $(i+1)$th grid point. Then, the volume flux at the $i+1/2$ grid point is also assigned the value zero. In the case shown in figure 18(b), however, the volume flux at the $i+1/2$ grid point is no longer zero. The new shoreline is located at the $i+1$ grid point. After the total depth has been updated from the continuity equation, the following algorithm is used to determine whether or not the shoreline should be moved. If $H_i > 0$, the possible cases can be summarized as follows.

If $H_{i+1} \leqslant 0$ and $h_{i+1} + \eta_i \leqslant 0$, then the shoreline remains between grid point i and $i+1$ and the volume flux $P_{i+1/2}$ remains zero.

If $H_{i+1} \leqslant 0$ and $h_{i+1} + \eta_i > 0$, then the shoreline moves to between grid points $i+1$ and $i+2$. The volume flux $P_{i+1/2}$ may have a non-zero value, while $P_{i+3/2}$ is assigned the value zero. The flooding depth is $H_f = h_{i+1} + \eta_i$.

If $H_{i+1} > 0$, then the shoreline moves to between grid points $i+1$ and $i+2$. The volume flux $P_{i+1/2}$ may also have a non-zero value, while $P_{i+3/2}$ is zero. The flooding depth is $H_f = \max (h_{i+1} + \eta_i, h_{i+1} + \eta_{i+1})$.

In the above cases, the time-step index has been omitted for simplicity. The algorithm works for both flooding and receding shoreline cases. The algorithm is developed for a two-dimensional problem and the corresponding y-direction algorithm has the same procedure as that for the x-direction.

To save computing time, the regions representing permanent dry (land) can be excluded from the computation by installing a depth criterion. Moreover, when H is very small, the associated bottom friction term will become large and, accordingly, the lower bound of water depth is used to avoid the difficulty.

B.2. The radiation boundary condition

The radiation boundary condition used in this study is an extension of the one-dimensional method of characteristics. For sinusoidal waves propagating in the positive x-direction (see figure 19a), the free-surface displacement η_o^{n+1} of open-boundary point o at time step $n+1$ can be approximated by the known value η_b^n at point b, since all the information at point b will be transferred to point p along the characteristic line $\overline{bp}$ if wave amplitude is small in comparison with local water depth h. The location of base point b, where the characteristic line starts, can be found as

$$l = (gh)^{1/2} \Delta t \tag{B 1}$$

and the free-surface displacement η_b^n at base point b can be interpolated linearly using the known values η_a^n and η_o^n at points a and o, respectively, as

$$\eta_b^n = \eta_a^n + \left(1 - \frac{l}{\Delta x}\right)(\eta_o^n - \eta_a^n) \tag{B 2}$$

and

$$\eta_o^{n+1} = \eta_b^n. \tag{B 3}$$

Similarly, the volume flux P_o^{n+1} can be found by

$$P_o^{n+1} = P_a^n + \left(1 - \frac{l}{\Delta x}\right)(P_o^n - P_a^n). \tag{B 4}$$

If the wave propagation direction is known locally along the open boundary, this one-dimensional method of characteristics can be extended to the two-dimensional case without great difficulty. It is assumed that the uniform waves propagate in the
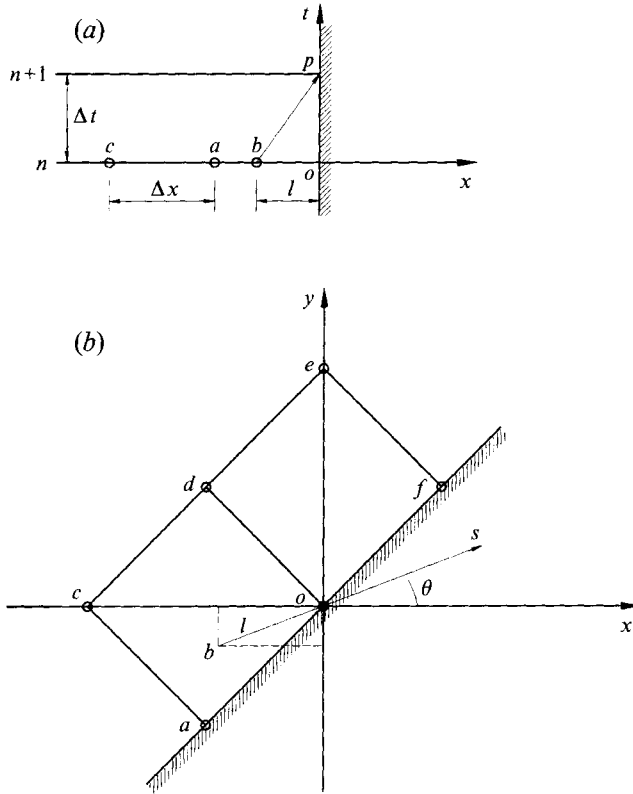
FIGURE 19. Radiation boundary condition: (a) one-dimensional radiation boundary;
(b) two-dimensional radiation boundary.

s-direction with angle θ with the x-direction (see figure 19b). The angle θ can be found by using the known values, i.e. P_o^n and Q_o^n, as

$$\theta = \tan^{-1}\left[\frac{Q_o^n}{P_o^n}\right]. \tag{B 5}$$

The coordinates are of the base point b, (x_1, y_1),

$$x_1 = -l\cos\theta, \qquad y_1 = -l\sin\theta. \tag{B 6}$$

Now the free-surface displacement η_b^n and the volume fluxes (P_b^n, Q_b^n) can be found by interpolating the values of the surrounding four points (i.e. o, a, c, and d). After interpolation, the following values are set:

$$\eta_o^{n+1} = \eta_b^n, \tag{B 7}$$

$$P_o^{n+1} = P_b^n, \qquad Q_o^{n+1} = Q_b^n. \tag{B 8}$$

When the free-surface displacement η_o^n is zero, the propagation angle θ is not defined. In this case the equation for θ can be replaced by

$$\theta = \tan^{-1}\left[\frac{\overline{Q}}{\overline{P}}\right] \tag{B 9}$$

where the overbar represents the values averaged over the adjacent points.

REFERENCES

AIDA, I. 1977 Numerical experiments for inundation of tsunamis, Susaki and Usa, in the Kochi Prefecture. *Bull. Earthq. Res. Inst.* **52**, 441–460 (in Japanese).

ARTHUR, R. S. 1946 Refraction of water waves by islands and shoals with circular bottom contours. *Trans. Am. Geophys. Union* **27**, 168–177.

BASCOM, W. 1990 *The Crest of the Wave – Adventures in Oceanography.* Doubleday, New York.

BRIGGS, M. J., SYNOLAKIS, C. E. & HARKINS, G. S. 1994 Tsunami run-up on a conical island. *Proc. of Waves – Physical and Numerical Modelling*, Vancouver, Canada.

CARRIER, G. F. 1966 Gravity waves in water of variable depth. *J. Fluid Mech.* **24**, 641–659.

CARRIER, G. F. & NOISEUX, C. F. 1983 The reflection of obliquely incident tsunamis. *J. Fluid Mech.* **133**, 147–160.

CHO, Y.-S. 1994 Numerical simulations of tsunami propagation and run-up. PhD thesis, Cornell University.

CHOW, V. T. 1959 *Open-Channel Hydraulics*, pp. 680. McGraw-Hill Book Company.

HIBBERD, S. & PEREGRINE, D. H. 1979 Surf and run-up on a beach: a uniform bore. *J. Fluid Mech.* **95**, 323–345.

HOKKAIDO TSUNAMI SURVEY GROUP 1993 Tsunami devastates Japanese coastal region. *EOS, Trans. AGU.* **74(37)**: 417 and 432.

HOUSTON, J. R. & BUTLER, H. L. 1979 A numerical model for tsunami inundation. *WES Tech. Rep.* HL-79-2.

IMAMURA, F., SYNOLAKIS, C. E., GIKA, G. & TITOV, V. 1995 The Midoro Island tsunami of November 15, 1994. *Pure Appl. Geophys.* (in press).

JONSSON, I. G. & SKOVGAARD, O. 1979 A mild-slope equation and its application to tsunami calculations. *Marine Geodesy* **2**, 41–58.

JONSSON, I. G., SKOVGAARD, O. & BRINK-KJAER, O. 1976 Diffraction and refraction calculations for waves incident on island. *J. Mar. Res.* **34**, 469–496.

KAJIURA, K. 1963 The leading wave of a tsunami. *Bull. Earthq. Res. Inst.* **41**, 535–571.

KANOGLU, U. 1995 The runup of long waves around piecewise linear bathymetries. PhD thesis, University of Southern California, Los Angeles, California.

KELLER, J. B. 1958 A geometrical theory of diffraction. In *Proc. Symposia in Appl. Maths*, vol. 8; *Calculus of Variations and its Applications* (ed. L. M. Graves), pp. 27–52. Am. Math. Soc.

KELLER, J. B. 1962 Geometric theory of diffraction. *J. Optical Soc. Am.* **52**, 116–130.

KELLER, J. B. & AHLUWALIA, D. S. 1973 Uniform asymptotic solution of eigenvalue problems for convex plane domains. *SIAM J. Appl. Maths* **25**, 583–591.

LAUTENBACHER, C. C. 1970 Gravity wave refraction by islands. *J. Fluid Mech.* **41**, 655–672.

LIU, P. L.-F. & CHO, Y.-S. 1994 An integral equation model for wave propagation with bottom frictions. *J. Waterway, Port, Coastal, Ocean Engng, ASCE* **120**, 594–608.

LIU, P. L.-F., YOON, S. B., SEO, S. N. & CHO, Y.-S. 1993 Numerical simulations of inundation at Hilo, Hawaii. *TSUNAMI '93. Proc. IUGG/IOC Intl Tsunami Symp.*, pp. 257–269, Japan.

MADER, C. L. & BERNARD, E. N. 1993 Modeling tsunami flooding of crescent city. *TSUNAMI '93. Proc. IUGG/IOC Intl Tsunami Symp.*, pp. 321–326, Japan.

POCINKI, L. S. 1950 The application of conformal transformation to ocean wave refraction problems. *Trans. Am. Geophys. Union* **31**, 856–860.

PROVIS, D. G. 1975 *Propagation of water waves near an island*. PhD thesis, University of Essex.

SATAKE, K., BOURGEOIS, J., ABE, K., TSUJI, Y., IMAMURA, F., IIO, Y., KATAO, H., NOGUERA, E. & ESTRADA, F. 1993 Tsunami field survey of the 1992 Nicaragua Earthquake. *EOS, Trans. AGU*, **74(13)**: 145, pp. 156–157.

SCHÄFFER, H. A. & JONSSON, I. G. 1992 Edge waves revisited. *Coastal Engng* **16**, 349–368.

SMITH, R. & SPRINKS, T. 1975 Scattering of surface waves by a conical island. *J. Fluid Mech.* **72**, 373–384.

SPRINKS, T. & SMITH, R. 1983 Scale effects in a wave-refraction experiment. *J. Fluid Mech.* **129**, 455–471.

SYNOLAKIS, C. E. 1987 The runup of solitary waves. *J. Fluid Mech.* **185**, 523–545.

SYNOLAKIS, C. E. 1990 Generation of long waves in the laboratory. *J. Waterways, Port, Coastal, Ocean Engng ASCE* **116**, 252–266.

SYNOLAKIS, C. E., IMAMURA, F., TINTI, S., TSUJI, Y., MATSUTOMI, H., COOK, B. & USMAN M. 1995 The East Java tsunami of June 4, 1994. *EOS, Trans.* AGU (In press).

TADEPALLI, S. & SYNOLAKIS, C. E. 1994 The run-up of N-waves on sloping beaches. *Proc. R. Soc. Lond.* A **445**, 99–112.

TAKAHASHI, T., IMAMURA, F. & SHUTO, N. 1993 Numerical simulation of topography change due to tsunamis. *TSUNAMI '93. Proc. IUGG/IOC Intl Tsunami Symp.*, pp. 243–256, Japan.

TITOV, V. & SYNOLAKIS, C. E. 1993 A numerical study of wave runup of the September 2, 1992 Nicaraguan tsunami. *TSUNAMI '93. Proc. IUGG/IOC Intl Tsunami Symp.*, pp. 627–636, Japan.

YEH, H. H., IMAMURA, F., SYNOLAKIS, C. E., TSUJI, Y., LIU, P. L.-F. & SHI, S. 1993 The Flores Island tsunamis. *EOS, Trans.* AGU **74(33)**: 369, pp. 371–373.

YEH, H. H., LIU, P. L.-F., BRIGGS, M. J. & SYNOLAKIS, C. E. 1994 Propagation and amplification of tsunamis at coastal boundaries. *Nature* **372**, 353–355.

YEH, H., TITOV, V., GUSIAKOV, V., PELINOVSKY, E., KHRAMUSHIN, V. & KAISTRENKO, V. 1995 The 1994 Shikotan earthquake tsunamis. *Pure Appl. Geophys.* (in press).